*Proceedings of the Thirty-fourth (2024) International Ocean and Polar Engineering Conference* **www.isope.org**
*Rhodes, Greece, June 16–21, 2024*

*ISBN 978-1-880653-78-4; ISSN 1098-6189*

# Simplified Structural Assessment of Ship Collision Against a Semisubmersible Offshore Wind Floater

*Priscilla Salazar L [(1)], Gabriel Vandegar [(1)], Ye Pyae Sone Oo [(2) (3)], Hervé Le Sourne [(2) (3)], Philippe Rigo [(1)]*

[(1)] Department of Naval and Structural Engineering (ANAST)
University of Liège, Belgium

[(2)] ICAM School of Engineering
Nantes Campus, France

[(3)] Nantes University, Ecole Centrale Nantes, CNRS, GeM Institute,
Nantes, France

## ABSTRACT

This work presents a simplified methodology to estimate the force-penetration curve for a large diameter cylindrical panel, corresponding to the structural arrangement in the outer tanks of a semisubmersible floater. The methodology is based on the upper-bound theorem of plastic limit analysis, accounting for membrane straining as the main mechanism for plastic deformation. The structural solver is coupled with a rigid-body dynamics subroutine to study the combined effects on the floater when it experiences a ship collision. Results are compared with nonlinear finite element simulations to investigate the applicability as a simpler and low-cost alternative for application during pre-design stages.

KEY WORDS: Ship collisions; floating offshore wind turbines; MCOL; super-element solver; cylindrical shells.

## INTRODUCTION

The advantages of floating offshore wind turbines (FOWT) regarding the exploitation of wind resources in deeper water are well-known to the date. The increase on floating offshore wind pipeline capacity by the end of 2023, shows that this type of technology is reaching the commercial phase, and the global number of floating farms is expected to grow shortly. This expansion would lead to a reduction on navigation space, an increase on traffic flow of service vessels and probably a rearrangement of navigation routes. Consequently, accounting for the risk of ship collisions against offshore wind turbines (OWT) is becoming more relevant during safety assessment. In the most recent events, in April 2023, a cargo ship collided with a wind turbine installed at the Gode Wind1 offshore wind farm (Orsted's Gode, 2023). In January 2022, a 37200 tons rudderless cargo ship drifted into the Hollandse Kust Zuid offshore wind farm in the Dutch North Sea during a storm (Hollandse Kust, 2023).

During the structural risk assessment, the accidental limit state (ALS) shall be checked not only considering the resistance to the accidental action but also the resistance in damaged condition caused by the accidental action (NORSOK N-001, 2012). Then, it is important to investigate local structural damages that could lead to the loss of integrity or performance of the structure.

The analysis of structural damage is studied by different approaches including empirical, experimental, and nonlinear finite element methods (NLFEM). Regarding the study of ship collisions against FOWT, an additional complexity is introduced since environmental loads influence the conditions for the event to occur, and the behavior of both structures during and after the impact.

Echeverry et al. (2019) studied the response of a spar-buoy FOWT collided by a ship using NLFEM software LS-DYNA jointly with MCOL external dynamics solver (Ferry et al., 2002). The influence of hydrodynamic forces was investigated showing that neglecting hydrodynamic loads led to a significant underestimation of the collision force. Zhang et al. (2021) studied the dynamic responses of a spar-buoy FOWT under accidental ship impact considering hydrodynamic, aerodynamic, and mooring loads in the collision model. The study focused primarily on the global motions of a spar FOWT and the resulting acceleration of the nacelle but neglects the deformation of the structure at the impact zone.

Yu et al. (2022) used the nonlinear finite element code USFOS to assess the response of a semisubmersible DTU 10 MW turbine supported by the OO-STAR concrete floater and impacted by a 7500 tons OSV. The approach considers the concrete column strong enough to avoid punching shear or flexural failure, then, only the ship is modeled as a deformable structure.

The abovementioned studies either disregard the structural deformation of the floater due to impact or employ NLFEM commercial software such as LS-DYNA to account for the energy dissipated by deformation and the corresponding contact force. Even when NLFEM approaches allow for a high-fidelity representation of the complex physical phenomena that take place in a ship-FOWT collision event, including large deformations, plasticity, complex contact, and fluid-structure interaction, such numerical analyses remain complex in terms of computation, expertise needed for model preparation and access to software. As an alternative, simplified methodologies to assess the structural damage for steel and concrete FOWT structures have been recently developed.

Marquez et al. (2022) proposed a simplified collision mechanical model to study ship impacts against reinforced concrete FOWTs. The study simulated a collision between a 3000 tons OSV and the ITI Energy barge using LS- DYNA/MCOL. The model correlated well to the NLFEM results in terms of structural penetrations, rigid-body motions, and contact force profiles, with a significantly lower computational cost compared against the NLFEM solutions.

Ladeira et al. (2023) developed a super-element (SE) solver to estimate the force-penetration curve of a standalone tubular OWT support. The approach considers an initial local elastic indentation at the contact zone, followed by a local plastic indentation combined with a global beam-like elastic bending, and a final buckling mechanism at the base of the tube. To simulate the response to impact against a spar-buoy FOWT, Vandegar et al. (2024) coupled the abovementioned solver with the rigid-body dynamics solver MCOL.

In the case of a semisubmersible floater, the structural components generally exposed to collisions are the three external columns (big-diameter cylindrical shells) and the truss structures that join them (tubular members or small-diameter cylindrical shells). Indentation and impact damage on small diameter cylindrical shells have been previously studied. Morris (1970) performed upper-bound calculations to estimate the plastic limit load for a thin cylindrical shell subjected to equal loads acting radially through a rigid body. Wierzbicki and Suh (1987) presented an analytical approach to determine the force-deflection relation for the local plastic indentation of tubes under lateral concentrated loads. Cerik et al. (2015) and Do et al. (2018) performed impact-tests on stiffened cylinders and compared with numerical simulations. They used knife-edge indenter, which defines the final deformed shape. The denting length at the impact region corresponds to the impactor width and the boundaries of the dent deform as semi-ellipses. It was shown that the plastic strain is concentrated at the impact region and how strain-rate effects become important for larger impact velocities. In Cerik (2015) a simplified method was also presented based on the model proposed by Wierzbicki and Suh (1987). In the work of Do et al. (2018) is also shown how the striker shape influences the energy absorbed by deformation, the most severe case being a hemispherical indenter which resembles a highly localized point loading.

Still, simplified analysis to study ship collision against semisubmersible steel FOWTs has not been developed up to the author's knowledge at the date of this publication.

This work aims to estimate the structural response of a cylindrical steel panel throughout the collision, i.e., to approximate a contact force-displacement curve, and the internal energy dissipated by deformation. An upper-bound approach for plastic limit analysis is applied to approximate the contact force causing structural collapse. This response is integrated with the solver MCOL which computes the rigid-body motion of the floater considering water inertial effects, hydrostatic restoring, and wave and viscous damping forces. The coupling allows to estimate a maximum penetration generated by the impact for different collision scenarios and a variety of structural characteristics.

Since various factors affecting the OWT performance are not considered in this study (e.g., environmental conditions, mooring lines, and turbine operation), this work does not intend to analyze the overall behavior of a semisubmersible structure due to ship collisions but to present a simplified approach to estimate the structural damage on a cylindrical steel panel and demonstrate that it can be easily integrated with other existing solvers. .

## SUPER-ELEMENT SOLVER

### Displacement field

In the application of the upper-bound theorem for plastic limit analysis, the first step is to construct a kinematically admissible displacement field $w(x,y)$, here defined in rectangular coordinate system. For this work, the displacement field is assumed to be described by a quadric surface (Eq.1). Coefficients $K_i$ are fitted by setting the surface boundaries with a group of parabolic functions as shown in Fig. 1. Along the $x$ coordinate, the central function $f_1(x)$ is known since it corresponds to the impactor shape displaced by the penetration $\delta$.

$$w(x,y) = K_0 + K_1 x + K_2 y + K_3 x^2 + K_4 xy + K_5 y^2 \quad (1)$$

On the other hand, $f_2(x)$ is unknown and its coefficients are obtained by defining the following as kinematic boundary conditions: the function's value and slope matches with $f_1(x)$ at the point $x_i$ and with the circular cross section function $g(x)$ at the point $x_f$. Since the curved panel is expected to be part of the full big diameter cylinder, the deformation extension $x_f$ is unknown as well as $x_i$. To solve the system of equations, a guess should be introduced regarding one of the unknown values: $g(x_f) = \delta/2$.

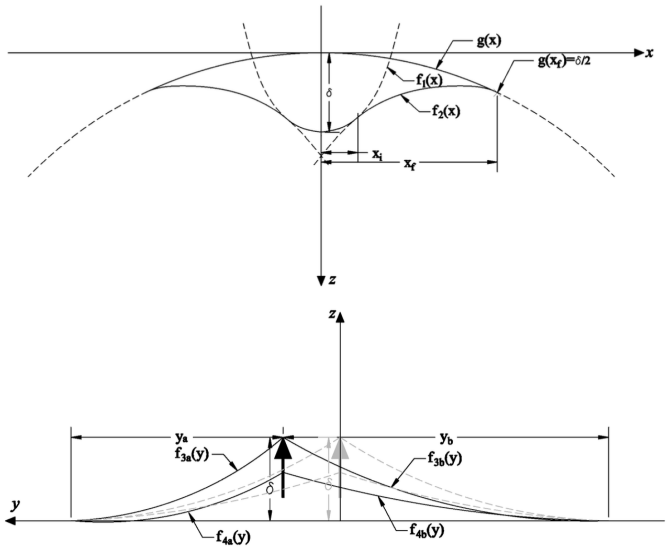


Fig. 1: Proposed displacement-field to describe the deformed curved panel surface. Upper figure: Top view of the deformed panel. Lower figure: Rotated lateral view of the deformed panel. Dashed lines show the displacement field for an impact point at the center and full lines for an eccentric load.

Along the $y$ coordinate, the function value for $f_{3a}(y)$ and $f_{3b}(y)$ at the impact point $y_0$ is equal to the penetration $\delta$. A zero slope is imposed at the impact point and at the boundaries. To maintain the simplicity of the approach, the complete deformed field is divided into four quadric surfaces ($w_1, w_2, w_3$ and $w_4$) with their own coefficients $K_i$:

$$w_1(x,y)\begin{cases}0 < x < x_i\\ 0 < y < y_a\end{cases} \qquad w_3(x,y)\begin{cases}x_i < x < x_f\\ 0 < y < y_a\end{cases}$$
$$w_2(x,y)\begin{cases}0 < x < x_i\\ -y_b < y < 0\end{cases} \qquad w_4(x,y)\begin{cases}0 < x < x_i\\ -y_b < y < 0\end{cases} \quad (2)$$

### Strain-displacement relation

Although the order of magnitude of the deformation analyzed exceeds the plate thicknesses' order of magnitude, assumptions are made based on the hypothesis of moderately large deformations to define the strain-displacement relations using the Green-Langrangian strain description. It is assumed that the plastic dissipation is well approximated using the plane strain assumption, then, out-of plane terms can be neglected. The in-plane component of the strain tensor[1] ($E_{\alpha\beta}$) is considered as shown

[1] Written in Einstein's summation convention

in Eq.3 with the index convention: $\alpha$ and $\beta$ = 1,2 and $k = 1,2,3$.

$$E_{\alpha\beta} = \frac{1}{2}\left[u_{\alpha,\beta} + u_{\beta,\alpha} + u_{k,\alpha}u_{k,\beta}\right] \tag{3}$$

The strain description is further simplified to Eq. 4 by presuming that the gradients of in-plane components of the displacement vector $u_i$ are negligible $\left(u_{1,\alpha}u_{1,\beta} \approx 0 \; and \; u_{2,\alpha}u_{2,\beta} \approx 0\right)$.

$$E_{\alpha\beta} = \frac{1}{2}\left[u_{\alpha,\beta} + u_{\beta,\alpha} + u_{3,\alpha}u_{3,\beta}\right] \tag{4}$$

The principal material coordinates coincide with the rectangular coordinate system defined for the displacement field, then $u_1$, $u_2$ and $u_3$ are the $x, y$ and $z$ components ($u, v$ and $w$) of the displacement vector. An additional simplification is introduced by stating that the panel deformation is mainly described by the transverse displacement $w$, i.e., changes in $u$ and $v$ along $x$ and $y$ axes are negligible, leading to a description compose only by the non-linear term in Eq. 5 and developed in Eq. 6.

$$E_{\alpha\beta} = \frac{1}{2}\left[u_{3,\alpha}u_{3,\beta}\right] \tag{5}$$

$$E_{\alpha\beta} = \frac{1}{2}\begin{bmatrix} -2z\dfrac{\partial^2 w}{\partial x^2} + \left(\dfrac{\partial w}{\partial x}\right)^2 & -2z\dfrac{\partial^2 w}{\partial x \partial y} + \left(\dfrac{\partial w}{\partial x}\dfrac{\partial w}{\partial y}\right) \\ -2z\dfrac{\partial^2 w}{\partial x \partial y} + \left(\dfrac{\partial w}{\partial x}\dfrac{\partial w}{\partial y}\right) & -2z\dfrac{\partial^2 w}{\partial y^2} + \left(\dfrac{\partial w}{\partial y}\right)^2 \end{bmatrix} \tag{6}$$

Finally, assuming that the plastic behavior of the deformed panel is governed by membrane strains, disregarding bending and twist, the components of the strain tensor to be considered are reduced to Eq. 7 and Eq. 8.

$$\epsilon_{xx} = \frac{1}{2}\left(\frac{\partial w}{\partial x}\right)^2 \tag{7}$$

$$\epsilon_{yy} = \frac{1}{2}\left(\frac{\partial w}{\partial y}\right)^2 \tag{8}$$

## Plastic dissipation and contact force

The equilibrium between the work done by external forces and the rate of energy dissipated by the plate's plastic deformation in a plane stress-strain condition and constant thickness $t$ is expressed in Eq. 9.

$$F\dot{\delta} = \iint_A \sigma_{\alpha\beta}\dot{\epsilon}_{\alpha\beta}\, t\, dA \tag{9}$$

Applying Huber-Mises yield condition for plane stress and its respective flow rule with flow stress $\sigma_0$, the equilibrium is defined as shown in Eq. 10. The velocity field is expressed in terms of the penetration rate (Eq. 11), then Eq. 12 and Eq. 13 take place in the radicand of Eq. 10 keeping in mind that the shape of the transverse displacement $w$ varies along with the polynomial coefficients' dependance on the penetration $\delta$, Eq. 14. The plastic strain is concentrated at the impact region, then, only $w_1$ and $w_2$ are considered.

$$F\dot{\delta} = \frac{2}{\sqrt{3}}\sigma_0\, t \int_y \int_x \sqrt{\dot{\epsilon}_{xx}{}^2 + \dot{\epsilon}_{xx}\dot{\epsilon}_{yy} + \dot{\epsilon}_{yy}{}^2}\, dx\, dy \tag{10}$$

$$\dot{w} = \dot{\delta}\frac{\partial w}{\partial \delta} \tag{11}$$

$$\dot{\epsilon}_{xx} = \frac{\partial}{\partial t}\left[\frac{1}{2}\left(\frac{\partial w}{\partial x}\right)^2\right] = \dot{\delta}\left(\frac{\partial w}{\partial x}\right)\frac{\partial}{\partial \delta}\left(\frac{\partial w}{\partial x}\right) \tag{12}$$

$$\dot{\epsilon}_{yy} = \frac{\partial}{\partial t}\left[\frac{1}{2}\left(\frac{\partial w}{\partial y}\right)^2\right] = \dot{\delta}\left(\frac{\partial w}{\partial y}\right)\frac{\partial}{\partial \delta}\left(\frac{\partial w}{\partial y}\right) \tag{13}$$

$$w(x, y, \delta) = K_0(\delta) + K_1(\delta)x + K_2(\delta)y + K_3(\delta)x^2 + K_4(\delta)xy + K_5(\delta)y^2 \tag{14}$$

## Validation

The contact force-penetration curve obtained with the super-element solver (SE solver), is compared with finite element simulations performed with the commercial software LS-DYNA. Since the approach is intended to be applied in the study of ship collisions against semisubmersible floaters, the cylinder geometry is selected in congruence with existing designs, shown in Table 1.

Table 1: Main characteristics of existing models for semisubmersible floaters

| Semisubmersible model | Radius (R) | Thickness (t) |
|---|---|---|
| OC4 (Robertson et al, 2014) | 6.00 m | 60 mm |
| WindFloat (Roddier et al, 2010) | 5.35 m | 30 mm |

***Finite element model***

The finite element model is prepared to perform simulations with software LS-DYNA.
A rigid bow impactor is set as a *PART_INERTIA with a total mass of 5000 tons. Given that the aim of this first part is to validate the force-displacement approximation, a displacement is imposed through the *BOUNDARY_PRESCRIBED_MOTION card. Belytschko-Tsay elements with five through-thickness integration points are used to model the impacted plate as recommended in Zhang et al. (2019). Piecewise linear plasticity model (MAT_024), with bi-linear consideration (Table 2) is applied for the impacted curved panel, and the rigid material (MAT_020) for the impactor bow shape. The strain-rate hardening effects are disregarded, a small value for the tangent modulus is used to approach the rigid-plastic material behavior assumed for the SE solver.

To study the convergence of results with respect to the element size, the curved panel is modeled using WindFloat's cylinder radius, thickness, and panel height as specified in Table 1. Half of the cylinder is modeled for the convergence study (Fig. 2) and the panel's boundary conditions are set as fixed on the four edges.

Table 2: Material properties used to model the curved panel in the numerical analysis.

| $\rho\ (kg/m^3)$ | $\sigma_y\ (MPa)$ | $E\ (GPa)$ | $E_{tan}\ (GPa)$ (tangent modulus) |
|---|---|---|---|
| 8500 | 364 | 207 | 5.5 |

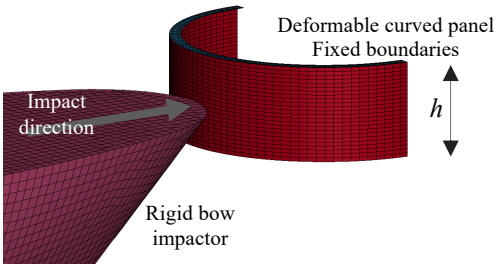


Fig. 2: NLFEM representation for ship impact against a curved panel with fixed boundaries and panel height $h$.

Five target element sizes were tested ranging from 5 to 75 cm, showing minor differences in the response for contact force as well as internal energy for element sizes in the range from 5 to 25 cm, Fig. 3. Then, the element size is set to 25 cm for the following comparisons.

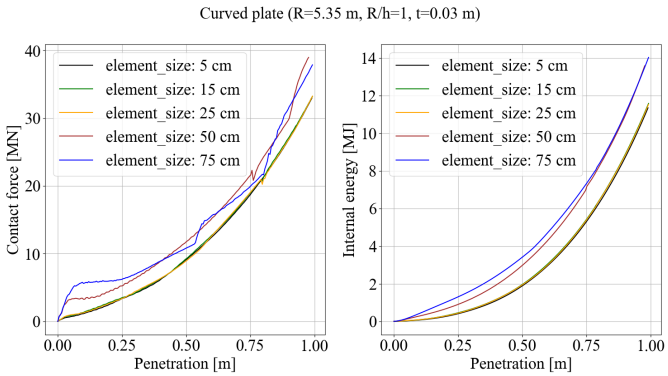


Fig. 3: Element size analysis for the curved plate

***Results and discussion***

The force-penetration curve for a curved plate with radius 5.35 m and thickness 30 mm is presented in Fig. 4. The results obtained by the super-element solver (full lines) correlate fairly well with the NLFEM solver (dashed lines) for moderately large penetrations and lower $R/h$ relation where $h$ is the plate height.

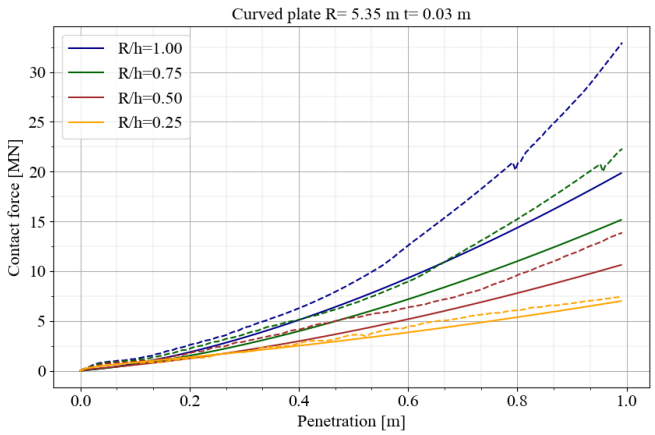


Fig. 4: Force-penetration curve estimation for different radius/plate heigh relation $(R/h)$ for the same radius and thickness (5.35 m and 30 mm respectively). Full lines: SE solver, dashed lines: NLFEM.

As shown in Table 3, the SE solver is able to predict the contact force with a discrepancy less than 15% for the smaller $R/h$ relation (equal to 0.25), however , the discrepancy increases to around 40% for the highest value studied.

Table 3: Comparison of contact force results obtained with NLFEM and SE solver for different penetrations and $R/h$ relations.

| Penetration (m) | Discrepancy in contact force between NLFEM and SE solver | | | |
|---|---|---|---|---|
| | R/h=1.00 | R/h=0.75 | R/h=0.50 | R/h=0.25 |
| 0.1 | 39% | 37% | 36% | 5% |
| 0.2 | 28% | 32% | 30% | 10% |
| 0.3 | 23% | 28% | 30% | 2% |
| 0.4 | 19% | 23% | 28% | 9% |
| 0.5 | 20% | 19% | 25% | 13% |
| 0.6 | 26% | 20% | 19% | 13% |
| 0.7 | 30% | 25% | 16% | 14% |
| 0.8 | 31% | 27% | 19% | 11% |
| 0.9 | 36% | 30% | 22% | 8% |
| 1.0 | 40% | 32% | 23% | 6% |

Note that the discrepancies between the numerical and SE solver results are calculated as:

$$Discrepancy = \frac{(Numerical - SE\ solver)}{Numerical} \tag{15}$$

For values of $R/h$ between 0.5 and 1, there is an initial elastic behavior on the curved plate that is not accounted for by the SE solver as the material is assumed to be rigid plastic. Young et al. (2012) presented an empirical solution for small radial deflections on cylindrical shells subjected to a concentrated load (Eq.16). Fig. 5 focus on the force-penetration curve for small values got from NLFEM results (dashed lines), compared with this small deformation empirical formula (dotted line).

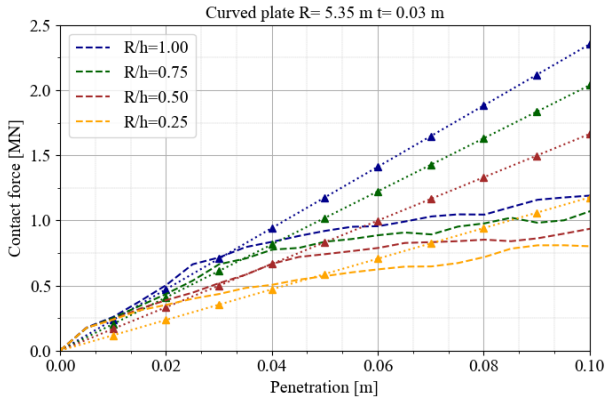


Fig. 5: Zoom in force-penetration curve for small penetrations at different radius/plate heigh relation $(R/h)$ comparing NLFEM results (dashed lines) with Young et al. (2012) approximation (dotted line with triangle markers).

By including the elastic response for small deflections, the contact force response is improved for moderately large deflections, still major discrepancies remain for penetrations higher than 0.6 m. However, the

elastic limit in terms of penetration is set by observation of NLFEM results, then, to integrate this elastic phase in the SE solver, further investigation is needed.

$$\delta = \frac{F}{Et}\left[0.48\left(\frac{h}{R}\right)^{1/2}\left(\frac{R}{t}\right)^{1.22}\right] \quad (16)$$

Table 4: Comparison of contact force results obtained with NLFEM and SE solver + elastic response for different penetrations and $R/h$ relations.

| Penetration (m) | Discrepancy in contact force between NLFEM and SE solver | | |
|---|---|---|---|
| | R/h=1 | R/h=0.75 | R/h=0.50 |
| 0.1 | 20% | 16% | 17% |
| 0.2 | 1% | 5% | 2% |
| 0.3 | 7% | 11% | 13% |
| 0.4 | 8% | 11% | 16% |
| 0.5 | 12% | 10% | 16% |
| 0.6 | 21% | 13% | 11% |
| 0.7 | 26% | 20% | 10% |
| 0.8 | 28% | 24% | 14% |
| 0.9 | 33% | 27% | 17% |
| 1.0 | 38% | 29% | 20% |

## COUPLING WITH MCOL SOLVER

To show the applicability of the developed solver in ship collisions and its easiness to be coupled with existing programs, the solution is integrated with the rigid-body dynamics solver MCOL. The semisubmersible's rigid-body motion is obtained by solving an equation of motion (Eq. 17) in the time domain including wave radiation damping forces $F_W$, hydrostatic restoring forces $F_H$, drag damping forces $F_V$ and contact forces $F_C$. The mass $M$ and gyroscopic $G$ matrices account for the contribution of dry rigid-body and water added mass at infinite frequency. Further details on the solution of Eq. 17 can be found in Ferry et al. (2002).

$$M\dot{y} + Gy = [F_W + F_H + F_V](y, x) + F_C \quad (17)$$

Following the approach explained in Vandegar et al. (2024) and initially elaborated by Marquez et al. (2022), the internal mechanics is integrated with the external dynamics by successively calling the super-element (SE) solver developed in this work for curved plates. A scheme of the algorithm implemented for the coupling is shown in Fig. 6. At the preliminary state, the algorithm is initialized with no penetration (initial contact force $F_c = 0$) locating the ship bow to be in contact with the curved plate.

In the next step, an initial penetration $\delta$ of the ship is calculated assuming no motion in the floater, then, it depends only on the ship velocity $v_{ship}$ and the selected time step $\Delta t$. The contact force $F_c(\delta)$ is estimated by applying Eq. 10. It is worth to note that the ship movement is restricted to x-direction, as well as the penetration (Fig. 7). The moments associated to the contact force are estimated by applying the cross product of the vectors $\overrightarrow{F_C}$ (only x-component) and from the floater's center of gravity to the contact point. These values are used to solve the equation of motion with MCOL solver and update the floater's kinematics to be used in the next time step. On the other hand, the ship kinematics are updated from the acceleration reduction due to the contact force. The increment on penetration $\Delta\delta$ to be used in the next time step is calculated from the relative velocity between the two bodies. The procedure is repeated over time until there is no more contact.

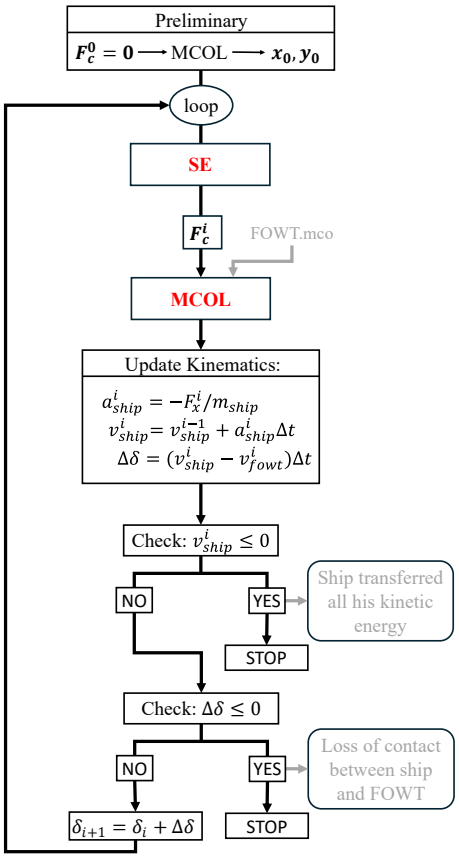


Fig. 6: Flow chart describing the methodology developed to couple Super-Element and MCOL solvers.

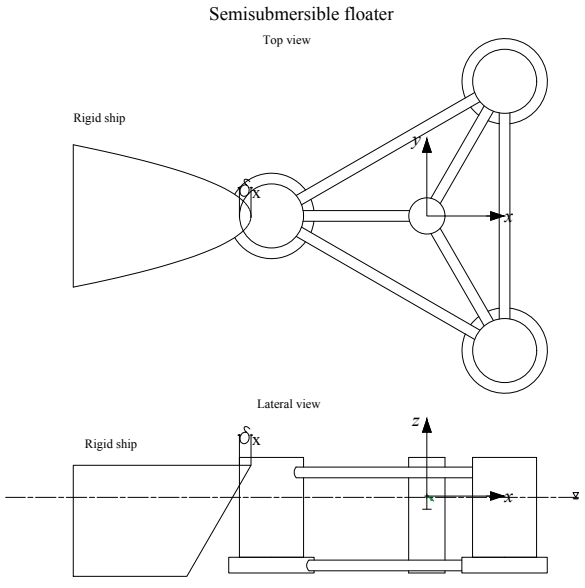


Fig. 7: Semisubmersible floater scheme, top and lateral view showing the selected coordinate system with origin at the center of gravity.

CASE STUDIES

## Floater characteristics

To test the SE solver coupled with MCOL, the semisubmersible structure used as reference was developed as part of the COL-L-FOWT project from the Walloon Region (Plan Marshall- GreenWin-Belgium) 2021–2023. The hydrodynamic characteristics of the semisubmersible floater (i.e., water added mass $M_\infty$, and frequency dependent wave damping matrices) were computed by DN&T company (Liège-Belgium) as part of the mentioned project employing the software FINE$^{TM}$/Marine and Ansys® Aqwa. These values are stored into the so-called FOWT.mco file needed to solve the rigid-body motion problem (Fig. 6). Due to confidentiality, only the main characteristics of the structure needed to perform the analysis are exposed in Table 5.

Table 5: Main dimensions of the semisubmersible floater used as reference. (COL-L-FOWT project from the Walloon Region).

| | |
|---|---|
| Cylinder radius (R) | 7.5 m |
| Plate height (h)<br>(Distance between internal decks) | 3.6 m |
| Plate thickness (t) | 30 mm |
| Total mass (floater+tower+turbine) | 13500 tons |

## Finite element model

Same as the procedure followed in the previous section to validate the force-displacement approximation, a finite element model prepared with LS-DYNA software is employed to validate the SE-MCOL coupling. The structural model of the cylinder is the same as described before and an additional rigid part is modeled at the floater's center of gravity and connected through rigid beams to the deformable half cylinder part. This additional rigid part is set as *PART_INERTIA containing the complete structure's characteristics (i.e., floater, tower, and turbine) regarding mass, inertia, and center of gravity. It is included in the external dynamics analysis using the *BOUNDARY_MCOL card.
Like in the previous section, the impactor is a rigid bow set as a *PART_INERTIA with a total mass of 5000 tons (assuming that this value includes the surge water added mass of the ship).

## Results and discussion

The coupling SE-MCOL is tested for impact velocities equal to 0.5, 1, 2 and 5 m/s. In addition, three impact locations were tested along the plate height: $0.5\,h$ (the midpoint of the plate height) $0.7h$ and $0.9h$ (at 70% and 90% of the plate height), being the latter the closer to the upper plate boundary. The outputs to compare are the maximum penetration and the maximum energy absorbed by deformation of the structure. These outputs are selected since the main intention of the development is to provide a simplified tool to evaluate the structural damage of the semi-submersible to be accounted on safety assessments. The results and differences between SE solver and NLFEM are presented on Table 6. For all the cases, the energy absorbed by deformation with respect to the impact energy is between 65-75%, showing the importance to be considered during a collision event. However, it is worth to remind that for this analysis the impactor ship is assumed as rigid, and the energy distribution will vary depending on the deformability of the impactor. The differences on internal energy for the lower velocity (Table 6) are between 14 and 19% for all the impact points studied. This difference can be explained since the SE solver does not account for the structural elastic recovery, which is not negligible at low velocities.

Table 6: Comparison of deformation energy and maximum penetration results obtained with NLFEM and SE solver for different impact velocities and locations along the plate height.

| **Impact velocity 0.5 m/s (impact energy 0.625 MJ)** | | | |
|---|---|---|---|
| **Deformation energy (MJ)** | | | |
| **Impact point** | **NLFEM+MCOL** | **SE+MCOL** | **DIFFERENCE** |
| 0.5h | 0.422 | 0.496 | 17% |
| 0.7h | 0.417 | 0.496 | 19% |
| 0.9h | 0.436 | 0.497 | 14% |
| **Maximum penetration (m)** | | | |
| **Impact point** | **NLFEM+MCOL** | **SE+MCOL** | **DIFFERENCE** |
| 0.5h | 0.249 | 0.261 | 5% |
| 0.7h | 0.226 | 0.245 | 9% |
| 0.9h | 0.145 | 0.180 | 24% |
| **Impact velocity 1 m/s (impact energy 2.5 MJ)** | | | |
| **Deformation energy (MJ)** | | | |
| **Impact point** | **NLFEM+MCOL** | **SE+MCOL** | **DIFFERENCE** |
| 0.5h | 1.820 | 1.986 | 9% |
| 0.7h | 1.822 | 1.988 | 9% |
| 0.9h | 1.799 | 1.993 | 11% |
| **Maximum penetration (m)** | | | |
| **Impact point** | **NLFEM+MCOL** | **SE+MCOL** | **DIFFERENCE** |
| 0.5h | 0.463 | 0.466 | 1% |
| 0.7h | 0.422 | 0.437 | 4% |
| 0.9h | 0.269 | 0.317 | 18% |
| **Impact velocity 2 m/s (impact energy 10 MJ)** | | | |
| **Deformation energy (MJ)** | | | |
| **Impact point** | **NLFEM+MCOL** | **SE+MCOL** | **DIFFERENCE** |
| 0.5h | 7.463 | 7.949 | 7% |
| 0.7h | 7.427 | 7.938 | 7% |
| 0.9h | 7.329 | 7.967 | 9% |
| **Maximum penetration (m)** | | | |
| **Impact point** | **NLFEM+MCOL** | **SE+MCOL** | **DIFFERENCE** |
| 0.5h | 0.795 | 0.823 | 4% |
| 0.7h | 0.726 | 0.771 | 6% |
| 0.9h | 0.465 | 0.556 | 20% |
| **Impact velocity 5 m/s (impact energy 62.5 MJ)** | | | |
| **Deformation energy (MJ)** | | | |
| **Impact point** | **NLFEM+MCOL** | **SE+MCOL** | **DIFFERENCE** |
| 0.5h | 46.42 | 49.67 | 7% |
| 0.7h | 45.88 | 49.70 | 8% |
| 0.9h | 39.62 | 49.94 | 26% |
| **Maximum penetration (m)** | | | |
| **Impact point** | **NLFEM+MCOL** | **SE+MCOL** | **DIFFERENCE** |
| 0.5h | 1.235 | 1.734 | 40% |
| 0.7h | 1.110 | 1.623 | 46% |
| 0.9h | 0.785 | 1.166 | 49% |

This behaviour can be observed on the energy balance in Fig. 8 looking at the internal energy dissipated ($W_{contact}$ in the figure). The effect becomes less important while the impact velocity increases as observed on Fig. 9, diminishing the discrepancy except for the cases where the impact point is close to the upper boundary $(0.9h)$ where other effects neglected on the SE solver could be influencing this response and should be further analysed (e.g., shear stresses). In addition, for low velocities, the overestimation of internal energy causes an underestimation on the floater's kinetic energy $K_{floater}$ and work done by hydrodynamic forces $W_{hydro}$ after the contact finishes.

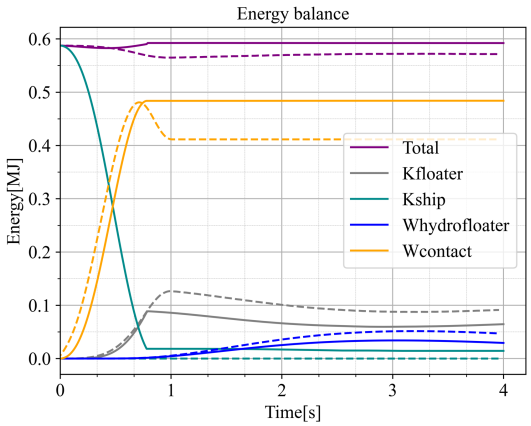


Fig. 8: Energy balance during and after contact for a collision with impact velocity of 0.5 m/s and impact point at the mid plate height.

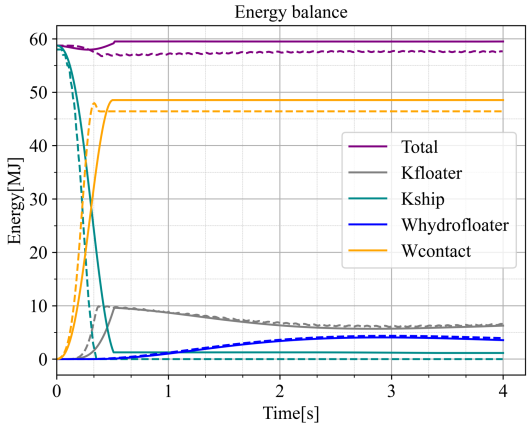


Fig. 9: Energy balance during and after contact for a collision with impact velocity of 5 m/s and impact point at the mid plate height.

Similar to the deformation energy, the differences shown on Table 6 for maximum penetration remain acceptable (less than 10%) except for the cases where the impact point is close to the upper boundary $(0.9h)$. Major differences (up to 49%) are found for the studied cases with higher impact velocity (5 m/s). These differences match with the discrepancies found in Table 4 when the SE solver was presented. As explained before, at higher penetration and higher $R/h$ ratio, the discrepancies in comparison with NLFEM results are more evident. For the studied case, the impact velocity of 5 m/s causes penetrations above 1 m and the $R/h$ relation is 2, which is out of the range analysed where the maximum value was $R/h = 1$. The divergence on results is noted on Fig. 10 and Fig. 11.

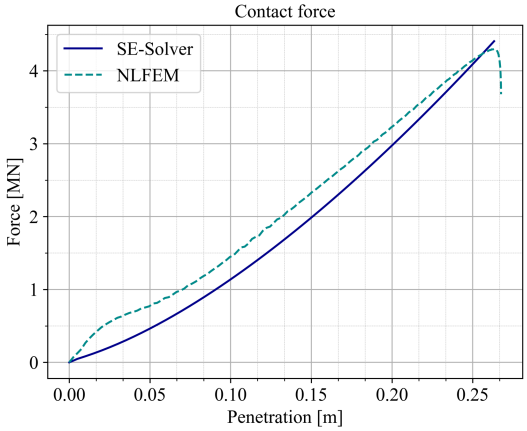


Fig. 10: Force-penetration curve for a collision against the studied semisubmersible with impact velocity of 0.5 m/s and impact point at the mid plate height. Full lines: SE solver, dashed lines: NLFEM.

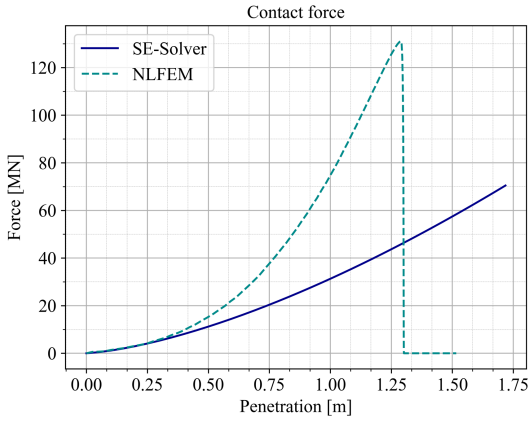


Fig. 11: Force-penetration curve for a collision with impact velocity of 5 m/s and impact point at the mid plate height. Full lines: SE solver, dashed lines: NLFEM.

## CONCLUSIONS

This study presents a simplified method to assess the local structural damage on a semisubmersible floater as consequence of a ship collision. The use of the simplified SE-Solver as an alternative to NLFEM to estimate the force-penetration curve on a curved plate is analyzed. The applicability and limitations for different cylinder characteristics are discussed showing the sensibility of the method to the plate's height. The contact force and internal energy obtained with the SE solver are integrated with the rigid body external dynamics solver MCOL showing its easiness to be combined with existing solvers to investigate coupled responses of semisubmersible FOWTs at different collision scenarios. Some investigations are on-going to improve the SE solver to better predict the FOWT damage at high impact velocities (5m/s and more).

## REFERENCES


Cerik, BC, Shin, HK, and Cho, S (2015). "On the resistance of steel ring-stiffened cylinders subjected to low-velocity mass impact," *International Journal of Impact Engineering 84, 108–123.*

Do, QT, Muttaqie, T, Shin, HK, and Cho, S (2018). "Dynamic lateral mass impact on steel stringer-stiffened cylinders," *International Journal of*

*Impact Engineering 116, 105–126.*

Echeverry, S, Marquez, L, Rigo, P, and Le Sourne, H (2019). "Numerical crashworthiness analysis of a spar floating offshore wind turbine impacted by a ship," *Proceedings of the 8th International Conference on Collision and Grounding of Ships and Offshore Structures, ICCGS 2019, 85–95.*

Ferry, M, Le Sourne, H, and Besnier, F (2002). "MCOL Theoretical Manual," *Principia Marine Technical Report.*

Hollandse Kust, (2022). "Rudderless Julietta D causes damage to foundation of wind farm Hollandse Kust. Zuid," *https://hollandsekust.vattenfall.nl/en/blog/2022/02/02/rudderless-julietta-d-causes-damage-to-foundation-of-wind-farm-hollandse-kust-zuid/.* Accessed: Jan 2024.

Ladeira, I, Echeverry, S and Le Sourne H (2023). "A simplified method to assess the elasto-plastic response of standalone tubular Offshore Wind Turbine supports subjected to ship impact," *Ocean Engineering 279 114313.*

Marquez, L, Le Sourne, H and Rigo, P (2022). "Mechanical model for the analysis of ship collisions against reinforced concrete floaters of offshore wind turbines," *Ocean Engineering 261 111987.*

Morris, AJ and Calladine, CR (1970). "Simple upper-bound calculations for the indentation of cylindrical shells," *J. Mech. Eng. Sci, 13, 331-343.*

NORSOK standard N-001 (2012). "Integrity of offshore structures"

Orsted's Gode Wind 1 (2023). "Cargo ship strikes turbine at Orsted's Gode Wind 1 offshore wind farm, suffers massive damage," *https://www.offshore-energy.biz/cargo-ship-strikes-orsteds-gode-wind 1-offshore-wind-farm-suffers-massive damage.* Accessed: Jan 2024.

Robertson, A, Jonkman, J, Masciola, M, Song, H, Goupee, A, Coulling, A, and Luan C (2014). "Definition of the semisubmersible floating system for phase II of OC4," *National Renewable Energy Laboratory (NREL) TP-5000-60.*

Roddier, D, Cermelli, C, Aubault, A, and Weinstein, A (2010) "WindFloat: A floating foundation for offshore wind turbines," *J. Renewable and Sustainable Energy 2, 033104.*

Vandegar, G, Sone Oo, YP, Ladeira, I, Le Sourne, H, and Echeverry, S (2024). "A simplified method to assess the elastoplastic response of standalone tubular Floating Offshore Wind Turbine supports subjected to ship impact," *Proceedings of the 9th International Conference on Collision and Grounding of Ships and Offshore Structures, ICCGS 2023, 447–454.*

Wierzbicki, T and Suh, MS (1945). "Indentation of tubes under combined loading," *International Journal of Mechanical Sciences 30, 229–248.*

Young, WC, Budynas, RG, and Sadegh, AM (2012). *Roark's Formulas for Stress and Strain.*

Zhang, S, Pedersen, PT, and Villavicencio, R (2019). "Collision damage assessment by nonlinear finite element simulations," *Probability and Mechanics of Ship Collision and Grounding.*